Research in Astronomy and Astrophysics, 25:085021 (8pp), 2025 August

https://doi.org/10.1088/1674-4527/ade65d
CSTR: 32081.14.RAA.ade65d

Wideband Polarized Emissions from PSR J1938+2213

Shu Ma[1], De-Hua Wang[1], Shuang-Qiang Wang[2,3,4], Fei-Fei Kou[2,4], Sheng-Nan Sun[2,4], and Na Wang[2,4]
[1] School of Physics and Electronic Science, Guizhou Normal University, Guiyang 550025, China; wangdh@gznu.edu.cn
[2] Xinjiang Astronomical Observatory, Chinese Academy of Sciences, Urumqi 830011, China; wangshuangqiang@xao.ac.cn
[3] CSIRO Astronomy and Space Science, PO Box 76, Epping, NSW 1710, Australia
[4] Xinjiang Key Laboratory of Radio Astrophysics, Chinese Academy of Sciences, Urumqi 830011, China
Received 2025 May 8; revised 2025 June 17; accepted 2025 June 19; published 2025 July 11

Abstract

We present a wideband polarization analysis of the mode-changing pulsar PSR J1938+2213 using the ultra-wideband low-frequency receiver on Murriyang, the Parkes 64 m radio telescope. Polarization profiles for both the burst and weak emission modes are obtained. We find that the pulse widths of the two modes exhibit distinct frequency dependencies: the pulse width increases with frequency in the burst mode, but decreases in the weak mode. The linear and circular polarization fractions also show different trends with frequency between the two modes. Our spectral analysis shows that both modes follow power-law spectra, but with differing spectral indices.

Key words: (stars:) pulsars: general – stars: neutron – methods: data analysis

1. Introduction

Pulsars are fast-rotating and highly magnetized neutron stars that produce beamed radio emission. The pulse energy of a pulsar fluctuates from pulse-to-pulse, however, the average pulse profile remains remarkably stable when a large number of single pulses are averaged (Taylor et al. 1975). It is generally suggested that the energy distribution of single pulses in a pulsar generally follows a log-normal or Gaussian distribution (Mickaliger et al. 2018). Some pulsars, however, exhibit a different type of intensity modulation, characterized by transitions between two or more stable modes. Pulse nulling of pulsars is the phenomenon where the pulsed emission abruptly disappears and later returns to the normal state (Backer 1970b). In observation, the duration of these nulls typically ranges from several pulses to several minutes, or even hours (Wang et al. 2007). In a few cases, the pulsed emission disappears for several days or even years, i.e., a behavior known as intermittent pulsars (Kramer et al. 2006a; Camilo et al. 2012; Lorimer et al. 2012; Lyne et al. 2017; Wang et al. 2020). Radio observations of pulsars simultaneously at different frequencies have shown that the nulling phenomenon is frequency-independent (Gajjar et al. 2014). Mode-changing is another phenomenon, in which the average pulse profile of a pulsar switches between two or more stable states, with mode durations ranging from several pulses to minutes or even hours (Bartel et al. 1982; Wang et al. 2007, 2024). The similar observational features suggest that nulling and mode-changing may share a common physical origin (Wang et al. 2007).

The mode-changing phenomenon was first discovered in PSR B1237+25 (Backer 1970a), and the subsequent observations have revealed mode-changing in dozens of pulsars. The observations of mode-changing provide an opportunity to study the radio emission mechanism of pulsars. Many theoretical models have been proposed to explain the mode-changing phenomena, however, the underlying mechanism causing pulsars to exhibit radio emission with different stable characteristics remains unclear. It was initially suggested that the mode-changing is associated with the sudden changes in current flows within the magnetosphere (Bartel et al. 1982). Timokhin (2010) proposed that the magnetospheres of some pulsars may exist different states, characterized by different geometries and/or current flow distributions, and mode-changing is detected when pulsars switch between these states. Lyne et al. (2010) found that six pulsars show the correlations between the timing noise and changes in the pulse shape, linking variations in the spin-down rate to changes in radio emission properties. This further supports the idea that mode-changing is related to the variations in magnetospheric current flows. Polarization observations have shown that the radio emissions in different modes of pulsars may originate from the same or different regions within the magnetosphere (Basu & Mitra 2018; Sun et al. 2022). Intensive studies of the radio emission properties of mode-changing pulsars, especially at multiple frequencies, are important for understanding the physical processes in the pulsar magnetosphere.

PSR J1938+2213 is a 166 ms pulsar that was discovered in the Arecibo 430 MHz drift-scan survey (Chandler 2003). It is a young pulsar with the characteristic age of 6.2×10^4 yr. Follow-up observations of this pulsar with Parkes telescope showed that its radio emission contains a stable weak mode superposed by brighter bursts (Lorimer et al. 2013). The bursting emissions are offset from the average profile of weak emissions in the pulse phase, and these bursting behaviors typically last for tens of

pulse periods. The emission properties of PSR J1938+2213 share some similarities with those of nulling pulsars, except that the pulse-to-pulse intensities are modulated by an abrupt decay into a null or weak state. A detailed single-pulse study with FAST suggests that the bright emissions are generated in different regions of the pulsar magnetosphere compared to the weak emission (Sun et al. 2022). Further wideband observations are critical for improving our understanding of the radio emission properties of PSR J1938+2213. In this paper, we present a multi-frequency radio observation of PSR J1938 +2213 using the ultra-wideband low-frequency (UWL) receiver on Murriyang, the Parkes 64 m radio telescope (Hobbs et al. 2020). We focus on investigating the radio emission properties of PSR J1938+2213 across a wide frequency range. In Section 2, we describe the observations and data processing. In Section 3, we present the observational results. In Section 4, we summarize and discuss our results.

2. Observations and Data Processing

We carried out an observation of PSR J1938+2213 with a duration of 3539 s using the UWL receiver on Murriyang, the Parkes 64 m radio telescope, with the Medusa backend (Hobbs et al. 2020). The observation was conducted on 2021 February 25, and search-mode data were recorded with 8-bit sampling, four polarizations, 3328 channels covering the full band, and a sampling interval of 128 μs. Prior to the pulsar observation, a 60 s calibration observation was recorded, during which a noise diode signal was injected into the feed.

For data analysis, we used the DSPSR software package (van Straten & Bailes 2011) to extract single pulses from the observation. The data consist of 26 subbands, and we removed 5 MHz from each edge of every subband. Radio-frequency interference was mitigated using the paz and pazi tools in the PSRCHIVE software package (Hotan et al. 2004). The calibration file was folded at the calibration pulse period, and the pulsar observation was calibrated using the pac tool in PSRCHIVE to flatten the bandpass and transform the polarization products into Stokes parameters. Observations of the radio galaxy 3C 218 (Hydra A) were used for absolute flux calibration. A detailed description of the UWL calibration procedure is given in Dai et al. (2019).

We used RMFIT to determine the rotation measure (RM) for our observation with a value of 140.14(9) rad m^{-2}, and subsequently corrected the data using the derived RM value. To study the emission properties across different frequencies, we divided the entire bandwidth into eight subbands, each with a bandwidth of 416 MHz, centered at 912, 1328, 1744, 2160, 2576, 2992, 3408, and 3824 MHz, respectively. PSRFLUX was used to measure the flux density in each subband. We calculated the fractional linear polarization (f_L) and the net circular polarization (f_V) of the average profiles for each subband, with uncertainties estimated using the baseline rms noise.

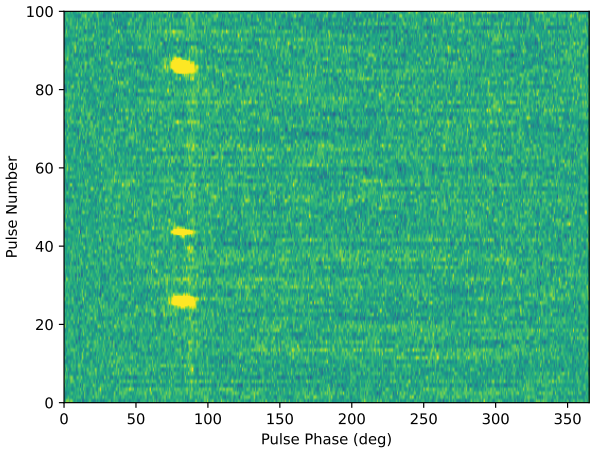

Figure 1. A single-pulse stack of 100 successive pulses from PSR J1938 +2213, in which the emission consists of a stable weak mode superimposed by bright bursts.

3. Results

3.1. Two Emission Modes

We obtained 21302 single pulses for PSR J1938+2213 in our observation. Considering that the signal-to-noise ratio of most single pulses is low, we refolded the data with a sub-integration of 10 single pulses, generating 2130 sub-integrations. A pulse stack of 100 successive pulses is shown in Figure 1, where the emission consists of a stable weak mode superposed by bright bursts.

We then calculated the on-pulse and off-pulse energies for each sub-integration. The on-pulse energy was determined by summing the intensities within the on-pulse window, which is defined as the longitude range in the average profile where the pulse intensity significantly exceeds the baseline noise. The off-pulse energy was calculated from a window of the same duration located in the baseline region. The distributions of on-pulse and off-pulse energies are shown in Figure 2, where the off-pulse energy follows a Gaussian distribution centered at zero, as expected. The on-pulse energy distribution shows a high-energy tail, corresponding to the bright burst emissions.

To classify the two modes, following the method of Bhattacharyya et al. (2010), we fitted a Gaussian function $N(E) = A\exp(-(E-\mu)^2/2\sigma^2)$ to the on-pulse energy distribution (Figure 2), where μ and σ are the mean and standard deviation, respectively, and A is a constant. We obtained $\mu = 0.34(1)$ and $\sigma = 0.75(1)$. If the on-pulse energy of a sub-integration is larger than $\mu + 3\sigma$ (i.e., 2.59), we classify it as the bright mode; otherwise, it is classified as the weak mode.

The frequency-averaged profiles of the burst and weak modes are shown in Figure 3. The profile of the weak mode shows two separated components, with the second component being brighter. The fraction of linear polarization is very high, about 95.5(1)%, while the fraction of circular polarization is

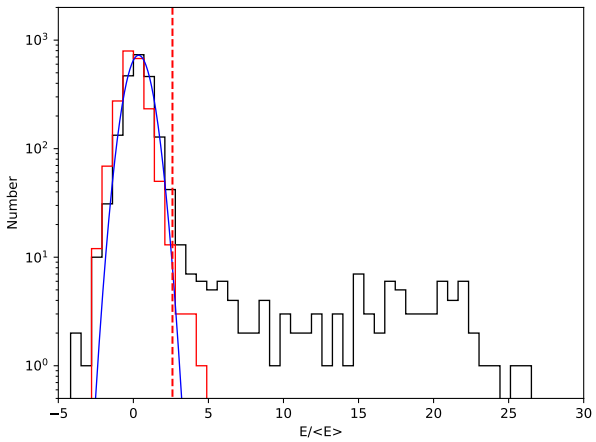

Figure 2. Pulse energy distributions for the on-pulse (black solid histogram) and off-pulse (red solid histogram) windows. The energy is normalized by the mean on-pulse energy. The blue line represents the Gaussian fit to the on-pulse energy distribution. The vertical dashed red line indicates the energy corresponding to 3σ of the fit.

low, about 9.6(4)%. The profile of the burst mode consists of three overlapping components, with the second component being the brightest. The first and third components coincide in the pulse phase with the two components of the weak mode. Similar to the weak mode, the circular polarization fraction remains low (about 1.5(4)%), but the linear polarization fraction decreases to about 45.4(4)%. Compared to the first and third components, the second component corresponds to a different orthogonal polarization mode. The peak intensity of the burst mode profile is approximately 24 times larger than that of the weak mode.

The orthogonal polarization mode (OPM) jumps are observed in the position angle (PA) swings during the burst mode of PSR J1938+2213 at pulse phases 75.°5 and 84.°0. These OPMs occur at phases where the linear polarization fraction drops to nearly zero. In contrast, the PA swing in the weak mode varies smoothly and closely resembles that of the burst mode, apart from the absence of OPM jumps. We performed Rotating Vector Model (RVM) fitting for both modes. According to the RVM (Radhakrishnan & Cooke 1969), the PA as a function of pulse longitude (ϕ) is given by:

$$\tan(\psi - \psi_0) = \frac{\sin\alpha \sin(\phi - \phi_0)}{\sin\zeta\cos\alpha - \cos\zeta\sin\alpha\cos(\phi - \phi_0)}, \quad (1)$$

where α is the angle between the rotation axis and the magnetic axis, $\zeta = \alpha + \beta$ is the angle between the rotation axis and the line of sight, and β is the impact angle (the closest approach of the magnetic axis to the line of sight). ψ_0 and ϕ_0 correspond to the PA and pulse phase at the inflection point of the PA swing, respectively. The RVM fitting yielded $\alpha_{\rm b} = 71^{+30}_{-34}$ deg, $\zeta_{\rm b} = 91^{+31}_{-42}$ deg, $\phi_{0,\rm b} = 87^{+3}_{-3}$ deg and $\psi_{0,\rm b} = -49^{+6}_{-7}$ deg for the burst mode, and $\alpha_{\rm w} = 108^{+38}_{-40}$ deg, $\zeta_{\rm w} = 126^{+31}_{-41}$ deg, $\phi_{0,\rm w} = 90^{+4}_{-4}$ deg and $\psi_{0,\rm b} = -58^{+13}_{-13}$ deg for the weak mode. For some pulsars, the OPM jump may be not exactly 90 deg, which may be due to propagation effects (e.g., Stinebring et al. 1984). Therefore, during the RVM fitting for the burst mode, we modeled the OPM jump as a free parameter and obtained a best-fit jump magnitude of 98^{+1}_{-1} deg, which does not deviate significantly from the typical 90°.

3.2. Frequency-dependent Polarization Profiles

To investigate the frequency dependence of the pulse profiles in different emission modes, we divided the full bandwidth into eight subbands, each with a bandwidth of 416 MHz. The polarization profiles for each mode at different frequencies are presented in Figure 4. The pulse width, fractions of linear, circular and absolute circular polarizations at different frequencies are shown in Figures 5 and 6, respectively.

In the burst mode, the first and third components are relatively weak compared to the second component but become more prominent with increasing frequency. The pulse width measured at 10% of the peak intensity (W10) initially decreases and then increases with frequency. The width at 50% intensity (W50) decreases from 912 MHz to 2160 MHz, then increases from 2576 MHz to 3824 MHz. This reversal is caused by the first component becoming stronger than half the peak intensity of the second component at higher frequencies. We note that the peak intensities of the first and third components are less than approximately 70% of the profile's peak intensity at all frequencies. Therefore, we also measured the W70 width, which corresponds only to the central component. The W70 initially decreases with frequency and then increases, indicating a non-monotonic frequency dependence. The linear polarization fraction ($f_{\rm L}$) initially increases and then decreases with frequency, ranging from 52(2)% to 29(4)%. Both the circular polarization ($f_{\rm V}$) and the absolute circular polarization ($f_{|\rm V|}$) remain low, around 2% across all subbands, with no clear frequency dependence.

In the weak mode, only the second component is clearly visible; the first component is too faint to be detected. As is typical for most pulsars, all W10, W50 and W70 decrease with increasing frequency. The linear polarization fraction is high, ranging from 86(4)% to 98(4)%, with no significant frequency dependence observed. Similar to the burst mode, $f_{\rm V}$ and $f_{|\rm V|}$ remain weak and do not exhibit any clear frequency-dependent behavior.

3.3. Spectrum

The flux densities at different frequencies for each mode are shown in Figure 7. As shown by Jankowski et al. (2018), the spectra of most pulsars can be modeled by a simple power law, although some pulsars show a high-frequency cutoff or low-frequency turnover. Based on the observed variation of flux density with frequency (Figure 7), we fitted the spectra using a

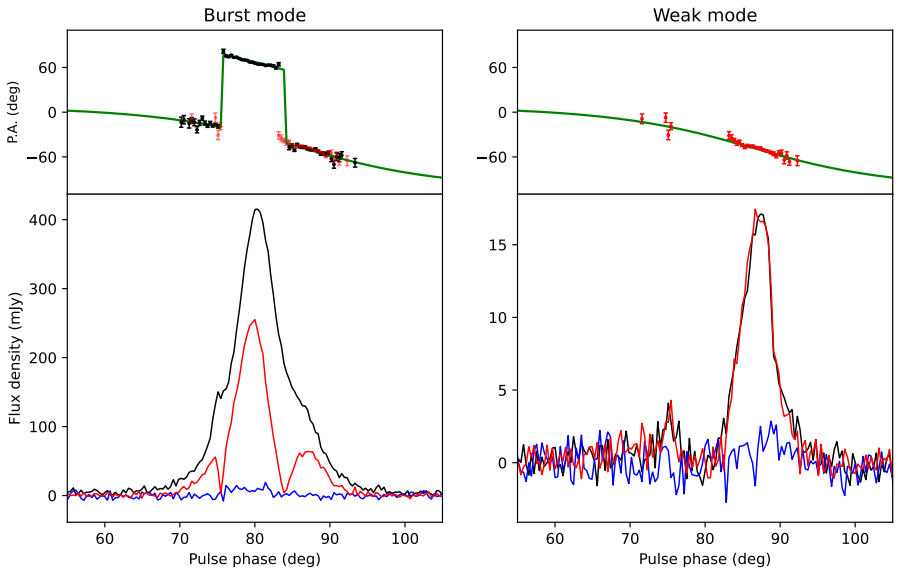

Figure 3. Frequency-averaged polarization profiles for the burst (left panel) and weak (right panel) modes. In each panel, the upper subpanel shows the PA swings of linear polarization: black dots for the burst mode and red dots for the weak mode. The green solid lines represent the best-fit RVM curves. The lower subpanel shows the total intensity (black line), linear polarization (red line), and circular polarization (blue line). For direct comparison, both the burst and weak mode PA swings are overplotted in the top left panel.

simple power law. The power-law model has the form:

$$S_\nu = bx^\alpha, \tag{2}$$

where $x = \nu/\nu_0$, ν is the observing frequency, $\nu_0 = 2368$ MHz is the reference frequency in our analysis, α is the spectral index, and b is a constant. The fitting results for both modes are shown in Figure 7. We found that the spectrum for both the burst and weak modes can be fitted by the power-law model well. The spectral indices of the burst and weak modes are different, with the values of $-1.43(6)$ and $-0.64(6)$, respectively. This indicates that the flux densities of the burst mode are more strongly frequency-dependent compared to those of the weak mode.

4. Discussion and Conclusions

We carried out a wideband observation of PSR J1938+2213 using the UWL receiver on the Parkes telescope to investigate its mode-changing behavior. Polarization profiles were obtained across a wide frequency range for both the burst and weak modes. In the frequency-averaged profiles, the peak intensity of the burst mode is approximately 24 times higher than that of the weak mode. Both modes exhibit notable frequency-dependent changes in pulse width. According to the radius-to-frequency mapping (RFM) model, lower-frequency emission originates from higher altitudes in the pulsar magnetosphere and thus exhibits broader profiles (Cordes 1978). This is a characteristic of coherent curvature radiation along diverging dipolar magnetic field lines (Gil et al. 2004). If the profile edges correspond to the last open field lines, the pulse width should follow RFM. However, polarization studies have shown that emission beams are generally underfilled (Johnston & Kramer 2019; Sun et al. 2025), implying that the observed profile edges may not trace the boundary of the open field line region. For PSR J1938 +2213, the weak mode pulse width decreases monotonically with increasing frequency, consistent with the RFM prediction. In contrast, the burst mode pulse width decreases at first but then increases at higher frequencies, suggesting that the emission beam in the burst mode is likely underfilled and more complex in structure. In addition, the pulse components may consist of unresolved subcomponents, which can affect the measurement of pulse width, such as W10 and W50 (Dai et al. 2015). Further observations with higher time resolution will be essential to resolve these individual components and may provide deeper insights into the frequency evolution of the pulse profile.

Our polarization analysis revealed the presence of OPMs in the burst mode but not in the weak mode. OPMs are thought to arise from propagation effects in the pulsar plasma (Barnard & Arons 1986; Petrova & Lyubarskii 2000; Beskin & Philippov 2012). In the burst mode, both ordinary (O-mode) and extraordinary (X-mode) components are present, whereas only a single mode (O- or X-mode) appears in the weak mode. This offers an opportunity to test propagation-based polarization models. Previous studies have proposed that the emission regions of the O-mode and X-mode become more overlapping at higher frequencies, leading to depolarization and a decrease in the linear polarization fraction (Petrova & Lyubarskii 2000;

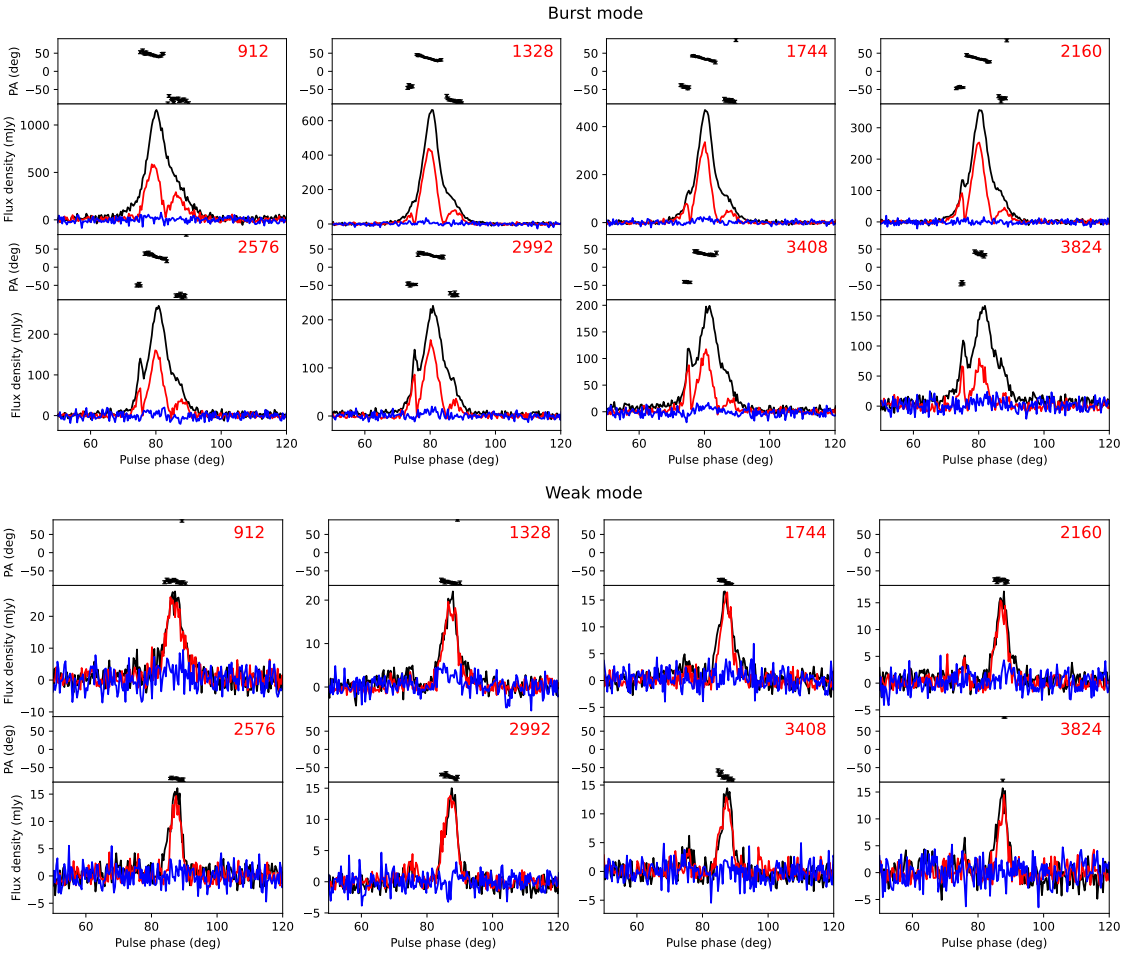

Figure 4. The polarization profiles for the burst (upper panel) and weak (bottom panel) modes at different frequencies. The central frequencies are indicated in red font. See Figure 3 for more details.

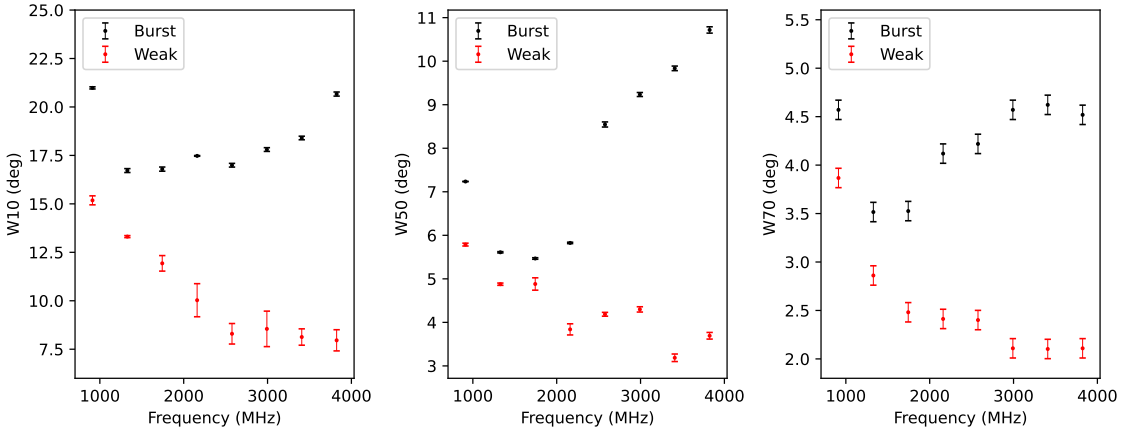

Figure 5. Pulse widths at 10% (left panel), 50% (middle panel) and 70% (right panel) peak intensities at different frequencies. The black and red dots represent the burst and weak modes, respectively.

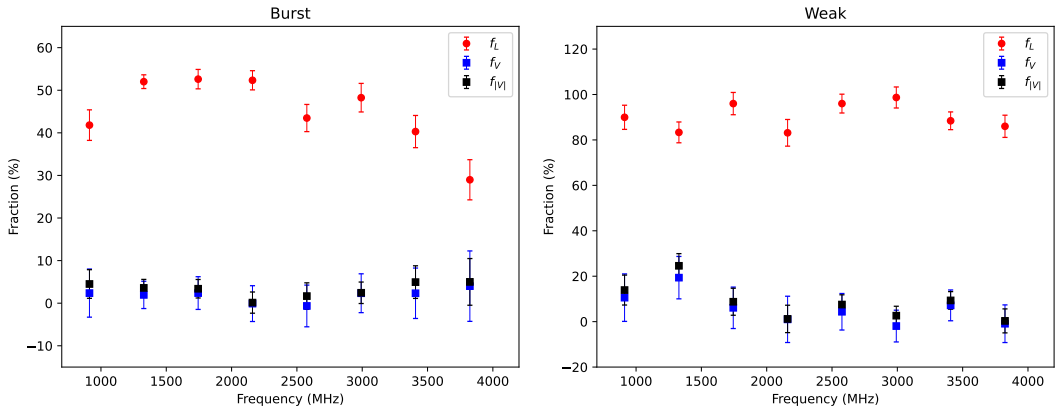

Figure 6. The fractions of linear, circular, and absolute circular polarizations at different frequencies for the burst (left panel) and weak (right panel) modes.

Wang et al. 2015; Wang & Han 2016). For the burst mode profile, which contains both O- and X-mode components, we observe a clear decrease in linear polarization fraction with increasing frequency. In contrast, the weak mode with only a single polarization mode, shows a consistently high linear polarization fraction with no significant frequency dependence. These results support the idea that depolarization at high frequencies arises from increasing overlap between O-mode and X-mode emission regions. The fact that OPMs are detected only in the burst mode further suggests differing local plasma conditions between the two modes. Overall, our findings are consistent with the interpretation that burst and weak mode emissions originate from distinct regions within the pulsar magnetosphere (Lorimer et al. 2013; Sun et al. 2022).

We performed RVM fitting for both the burst and weak modes of PSR J1938+2213 to investigate their magnetospheric geometry. For the burst mode, we obtained $\alpha_{\rm b} = 71^{+30}_{-34}$ deg and $\zeta_{\rm b} = 91^{+31}_{-42}$ deg, while for the weak mode, the values are $\alpha_{\rm w} = 108^{+38}_{-40}$ deg and $\zeta_{\rm w} = 126^{+31}_{-41}$ deg. These parameters come with large uncertainties, which are expected given the narrow pulse profiles, leading to strong covariance between α and β in the RVM fitting (Everett & Weisberg 2001). Despite the uncertainties, the similarity in PA swing variations and the consistency of α and ζ values within error bars suggest that the magnetospheric geometry remains unchanged between the two modes. According to Blaskiewicz et al. (1991), the centroid of the PA swing lags behind the centroid of the pulse profile due to relativistic effects such as aberration and retardation (A/R). In principle, the emission height can be estimated by accounting for A/R effects, assuming the observed pulse width is centered on the magnetic axis. However, emission beams are often underfilled in longitude (Johnston & Kramer 2019; Sun et al. 2025), complicating the measurement of the pulse centroid. Given this and the large uncertainties in α and ζ, we do not attempt to estimate the emission height here.

Mode-changing has been detected in many pulsars, yet its physical origin remains poorly understood. A correlation between timing noise and pulse shape (Lyne et al. 2010) suggests that mode-changing may result from variations in current flows within the magnetosphere. Timokhin (2010) proposed that pulsars may switch between different magnetospheric states with distinct current distributions or geometries. In pulsars with S-shaped PA swings, RVM fitting provides insights into geometry and emission height. In many cases, PA swings across different modes show similar behavior, indicating that the magnetospheric geometry remains constant (Basu & Mitra 2018; Rahaman et al. 2021). Thus, mode-changing is likely due to variations in current flows that reshape emission regions rather than alter global geometry. Polarization studies support this view but also reveal diversity: PSR J1822−2256 exhibits identical emission heights across modes (Basu & Mitra 2018), whereas PSR J0614+2229 shows differing heights (Sun et al. 2022). These findings suggest two classes of mode-changing pulsars: one with consistent emission heights, and the other with different heights across modes. Our RVM fitting indicates that PSR J1938+2213 belongs to the second class. While the geometry appears consistent between modes, the differing PA swing properties imply different emission regions.

We also analyzed the spectral properties of PSR J1938 +2213 in both modes and found that their spectra are well described by power-law models. The spectral index is -1.43 ± 0.06 for the burst mode and -0.64 ± 0.06 for the weak mode. Since the two modes are likely generated in different regions of the magnetosphere, the observed difference in spectral indices is expected. A similar result was found in PSR J0614+2229, where distinct emission regions are also associated with differing spectral indices (Zhang et al. 2020). Whether pulsars with the same emission heights exhibit similar or different spectral properties remains an open question. Continued wideband observations of mode-changing pulsars will help clarify the relationship between emission height and

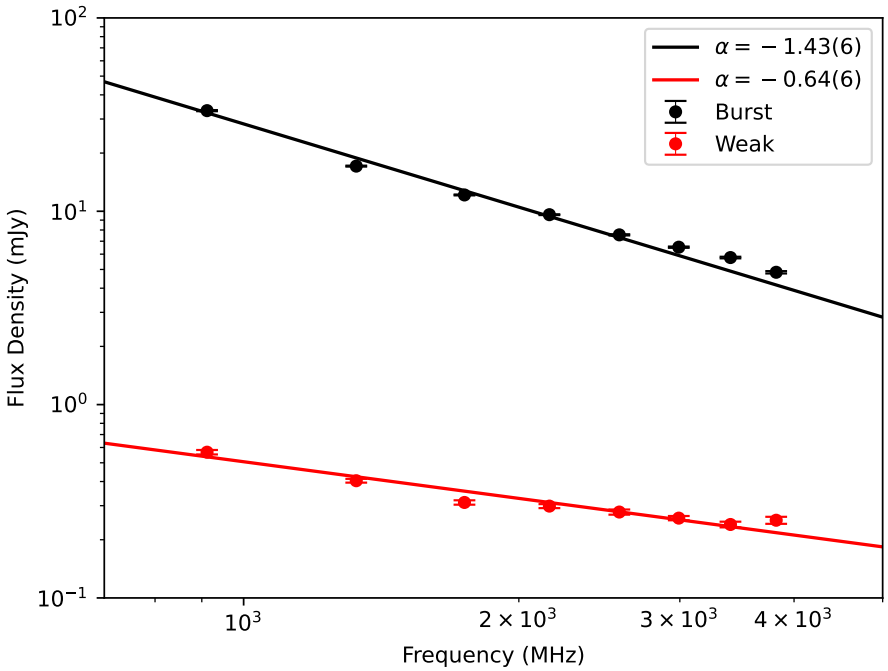

Figure 7. The flux densities of the burst (black dots) and weak (red dots) modes. The solid lines represent the fitting results using the power-law model.

spectral behavior, providing new constraints on pulsar emission physics.

Despite decades of study, the pulsar emission mechanism remains elusive. Competing models include curvature radiation (Buschauer & Benford 1976) and inverse Compton scattering (Qiao & Lin 1998). Simulations based on both mechanisms can reproduce key polarization features, such as sign reversals in circular polarization, strong linear polarization in some components, and the classic S-shaped PA swings (Xu et al. 2000; Wang et al. 2012, 2014). However, explaining the full range of observed properties, particularly the complex evolution of polarization across wide frequency bands (Sobey et al. 2021), remains a challenge (e.g., Wang et al. 2014). For mode-changing pulsars like PSR J1938+2213, studying the polarization evolution across frequencies in different modes could provide more valuable clues about emission processes. We plan to continue wideband polarization observations of pulsars using the UWL receiver on Parkes. These data will be crucial for conducting simulations that can better explain the diverse behaviors of pulsar emission, ultimately advancing our understanding of the underlying mechanisms.

Acknowledgments

We thank referee's valuable suggestions. This work is supported by the National Natural Science Foundation of China (Nos. 12288102, 12203092, 12041304, 12403060, 12203045, 12203093, 12163001 and 12463007), the Major Science and Technology Program of Xinjiang Uygur Autonomous Region (Nos. 2022A03013-3, and 2022A03013-2), the National SKA Program of China (No. 2020SKA0120100), the National Key Research and Development Program of China (Nos. 2022YFC2205202 and 2021YFC2203502), the Natural Science Foundation of Xinjiang Uygur Autonomous Region (Nos. 2022D01B71 and 2022D01B218), the Tianshan Talent Training Program for Young Elite Scientists (No. 2023TSYCQNTJ0024), the 2022 Project Xinjiang Uygur Autonomous Region of China for Tianchi Talents, the open research project funded by the Key Laboratory of Xinjiang Uyghur Autonomous Region (No. 2021000059), and the National Key Research and Development Program (No. 2022YFA1603104). The research is partly supported by the Operation, Maintenance and Upgrading Fund for Astronomical Telescopes and Facility Instruments, budgeted from the Ministry of Finance of China (MOF) and administrated by the Chinese Academy of Sciences (CAS). Murriyang, CSIRO's Parkes radio telescope, is part of the Australia Telescope National Facility (https://ror.org/05qajvd42) which is funded by the Australian Government for operation as a National Facility managed by CSIRO. We acknowledge the Wiradjuri people as the Traditional Owners of the Observatory site. This paper includes archived data obtained through the Parkes Pulsar Data archive on the CSIRO Data Access Portal (http://data.csiro.au).

References

Backer, D. C. 1970a, Natur, 228, 1297
Backer, D. C. 1970b, Natur, 228, 42
Barnard, J. J., & Arons, J. 1986, ApJ, 302, 138
Bartel, N., Morris, D., Sieber, W., & Hankins, T. H. 1982, ApJ, 258, 776

Basu, R., & Mitra, D. 2018, MNRAS, 476, 1345
Beskin, V. S., & Philippov, A. A. 2012, MNRAS, 425, 814
Bhattacharyya, B., Gupta, Y., & Gil, J. 2010, MNRAS, 408, 407
Blaskiewicz, M., Cordes, J. M., & Wasserman, I. 1991, ApJ, 370, 643
Buschauer, R., & Benford, G. 1976, MNRAS, 177, 109
Camilo, F., Ransom, S. M., Chatterjee, S., Johnston, S., & Demorest, P. 2012, ApJ, 746, 63
Chandler, A. M. 2003, Pulsar Searches: From Radio to Gamma-rays, PhD thesis, California Inst. Technology
Cordes, J. M. 1978, ApJ, 222, 1006
Dai, S., Hobbs, G., Manchester, R. N., et al. 2015, MNRAS, 449, 3223
Dai, S., Lower, M. E., Bailes, M., et al. 2019, ApJL, 874, L14
Everett, J. E., & Weisberg, J. M. 2001, ApJ, 553, 341
Gajjar, V., Joshi, B. C., Kramer, M., Karuppusamy, R., & Smits, R. 2014, ApJ, 797, 18
Gil, J., Lyubarsky, Y., & Melikidze, G. I. 2004, ApJ, 600, 872
Hobbs, G., Manchester, R. N., Dunning, A., et al. 2020, PASA, 37, e012
Hotan, A. W., van Straten, W., & Manchester, R. N. 2004, PASA, 21, 302
Jankowski, F., van Straten, W., Keane, E. F., et al. 2018, MNRAS, 473, 4436
Johnston, S., & Kramer, M. 2019, MNRAS, 490, 4565
Kramer, M., Lyne, A. G., O'Brien, J. T., Jordan, C. A., & Lorimer, D. R. 2006a, Sci, 312, 549
Lorimer, D. R., Camilo, F., & McLaughlin, M. A. 2013, MNRAS, 434, 347
Lorimer, D. R., Lyne, A. G., McLaughlin, M. A., et al. 2012, ApJ, 758, 141
Lyne, A. G., Stappers, B. W., Freire, P. C. C., et al. 2017, ApJ, 834, 72
Lyne, A., Hobbs, G., Kramer, M., Stairs, I., & Stappers, B. 2010, Sci, 329, 408
Mickaliger, M. B., McEwen, A. E., McLaughlin, M. A., & Lorimer, D. R. 2018, MNRAS, 479, 5413
Petrova, S. A., & Lyubarskii, Y. E. 2000, A&A, 355, 1168
Qiao, G. J., & Lin, W. P. 1998, A&A, 333, 172
Radhakrishnan, V., & Cooke, D. J. 1969, ApL, 3, 225
Rahaman, S. k. M., Basu, R., Mitra, D., & Melikidze, G. I. 2021, MNRAS, 500, 4139
Sobey, C., Johnston, S., Dai, S., et al. 2021, MNRAS, 504, 228
Stinebring, D. R., Cordes, J. M., Rankin, J. M., Weisberg, J. M., & Boriakoff, V. 1984, ApJS, 55, 247
Sun, S. N., Wang, N., Yan, W. M., & Wang, S. Q. 2025, ApJ, 983, 179
Sun, S. N., Yan, W. M., Wang, N., et al. 2022, ApJ, 934, 57
Taylor, J. H., Manchester, R. N., & Huguenin, G. R. 1975, ApJ, 195, 513
Timokhin, A. N. 2010, MNRAS, 408, L41
van Straten, W., & Bailes, M. 2011, PASA, 28, 1
Wang, N., Manchester, R. N., & Johnston, S. 2007, MNRAS, 377, 1383
Wang, P. F., & Han, J. L. 2016, MNRAS, 462, 4416
Wang, P. F., Wang, C., & Han, J. L. 2012, MNRAS, 423, 2464
Wang, P. F., Wang, C., & Han, J. L. 2014, MNRAS, 441, 1943
Wang, P. F., Wang, C., & Han, J. L. 2015, MNRAS, 448, 771
Wang, S. Q., Wang, J. B., Hobbs, G., et al. 2020, ApJ, 897, 8
Wang, S. Q., Wang, N., Wang, J. B., et al. 2024, ApJ, 964, 6
Xu, R. X., Liu, J. F., Han, J. L., & Qiao, G. J. 2000, ApJ, 535, 354
Zhang, Y. R., Wang, H. G., Huang, X. J., & Chen, J. L. 2020, ApJ, 890, 31